nature geoscience

ARTICLES

https://doi.org/10.1038/s41561-021-00717-0

Check for updates

Bedrock weathering contributes to subsurface reactive nitrogen and nitrous oxide emissions

Jiamin Wan[1]✉, Tetsu K. Tokunaga[1]✉, Wendy Brown[2], Alexander W. Newman[2], Wenming Dong[1], Markus Bill[1], Curtis A. Beutler[2], Amanda N. Henderson[2], Nydra Harvey-Costello[1], Mark E. Conrad[1], Nicholas J. Bouskill[1], Susan S. Hubbard[1] and Kenneth H. Williams[1,2]

Atmospheric nitrous oxide contributes directly to global warming, yet models of the nitrogen cycle do not account for bedrock, the largest pool of terrestrial nitrogen, as a source of nitrous oxide. Although it is known that release rates of nitrogen from bedrock are large, there is an incomplete understanding of the connection between bedrock-hosted nitrogen and atmospheric nitrous oxide. Here, we quantify nitrogen fluxes and mass balances at a hillslope underlain by marine shale. We found that, at this site, bedrock weathering contributes 78% of the subsurface reactive nitrogen, while atmospheric sources (commonly regarded as the sole sources of reactive nitrogen in pristine environments) account for only the remaining 22%. About 56% of the total subsurface reactive nitrogen denitrifies, including 14% emitted as nitrous oxide. The remaining reactive nitrogen discharges in porewaters to a floodplain where additional denitrification probably occurs. We also found that the release of bedrock nitrogen occurs primarily within the zone of the seasonally fluctuating water table and suggest that the accumulation of nitrate in the vadose zone, often attributed to fertilization and soil leaching, may also include contributions from weathered nitrogen-rich bedrock. Our hillslope study suggests that, under oxygenated and moisture-rich conditions, weathering of deep, nitrogen-rich bedrock makes an important contribution to the nitrogen cycle.

Nitrous oxide is produced during both microbial nitrification and denitrification in terrestrial and aquatic systems[1,2]. Predictions of N_2O production rates have been based on estimated rates of reactive nitrogen (reactive-N) inputs including N-fertilizers, manure, fossil-fuel combustion and natural atmospheric sources[2–6], without accounting for large quantities of weathering-released rock-N (refs. [7–11]). In pristine environments, atmospheric deposition and biological fixation in soils are still commonly regarded as the sole natural sources for reactive-N (refs. [12,13]), despite mounting evidence for the importance of rock-N release to surface waters from weathering[7–11]. Bedrock constitutes the largest terrestrial N reservoir on Earth, with fine-grained shale and mudstone containing the largest N inventory[7]. In these rocks, N is associated with organic matter, with post-burial diagenetic processes altering a fraction of the organic-N to ammonium (NH_4^+), which can be incorporated into silicate minerals and sorbed on clays[11,14,15]. Shales are recognized for their high capacity to release solutes including C, N and metals through chemical weathering[16,17]. Current understanding and models associated with rock weathering inputs to ecosystems rely on rates of tectonic uplift and land surface erosion[18–21] over long geological time scales. Determining regional and local bedrock-N weathering influxes to ecosystems is technically challenging[2], as is determining subsurface weathering rates. Additionally, there is a paucity of information on N_2O originating from transformations of bedrock-released N, although measured N_2O emissions from shale-derived soils indicate that this pathway is important[22].

Our study was conducted in the East River watershed[23] in the Upper Colorado River Basin (Fig. 1), along a lower montane hillslope (Fig. 1b,c) underlain with Mancos Shale[24]. This Cretaceous shale is broadly distributed throughout the southwestern United States, and releases elevated concentrations of major ions, trace elements and potential contaminants through chemical weathering[16,17]. Thus, shale weathering fluxes are dominant contributions to the East River's seasonally varying water chemistry[25–28]. Five boreholes (Fig. 1c–g) were drilled along a transect to obtain porewater and gas samples at different depths spanning the soil-to-bedrock continuum. Time-dependent hydrologic properties[27,28], including groundwater flow and water table depth, were also measured over three years. The annual total N input from atmospheric deposition measured at the Gothic CASTNET station[29] located 5 km from the hillslope is 2.68 ± 0.22 kg N ha^{-1} year^{-1}. Based on other work in the mountainous regions of Colorado[30], the biological N fixation (BNF) rate was assumed to be roughly equivalent to the deposition rate, and this value is about 10% lower than the estimated globally averaged terrestrial BNF rate of 3.0 kg N ha^{-1} year^{-1} (ref. [31]).

Weathering is controlled by water table depth

Rock-N reentry into the labile reactive-N pool warrants a brief summary of the subsurface weathering mechanisms along the hillslope. The average soil thickness along the hillslope of 1.0 ± 0.3 m was determined using a hand-auger. We applied the established method of quantifying weathering depths through relative concentration $\tau_{i,j}$[32,33] profiles of minerals (Methods). The profile average concentrations in the 4–10 m below ground surface (bgs) interval were used to calculate the $\tau_{i,j}$ profiles (excluding a hot spot in PLM1). The unweathered bedrock contains on average 3.0% pyrite, 4.6% calcite, 7.5% dolomite, 7% plagioclase and 30% illite. Pyrite, being ubiquitous in marine sedimentary rocks, is the most diagnostic mineral for weathering depth[34,35]. Pyrite and carbonates are completely depleted ($\tau_j = -1$) down to about 2.0 m bgs, and the weathering fronts ($\tau_j = {}_0$) are at approximately 3.8, 4.2 and 3.3 m bgs at locations PLM1, PLM2

[1]Earth and Environment Sciences Area, Lawrence Berkeley National Laboratory, Berkeley, CA, USA. [2]Rocky Mountain Biological Laboratory, Crested Butte, CO, USA. ✉e-mail: jwan@lbl.gov; tktokunaga@lbl.gov

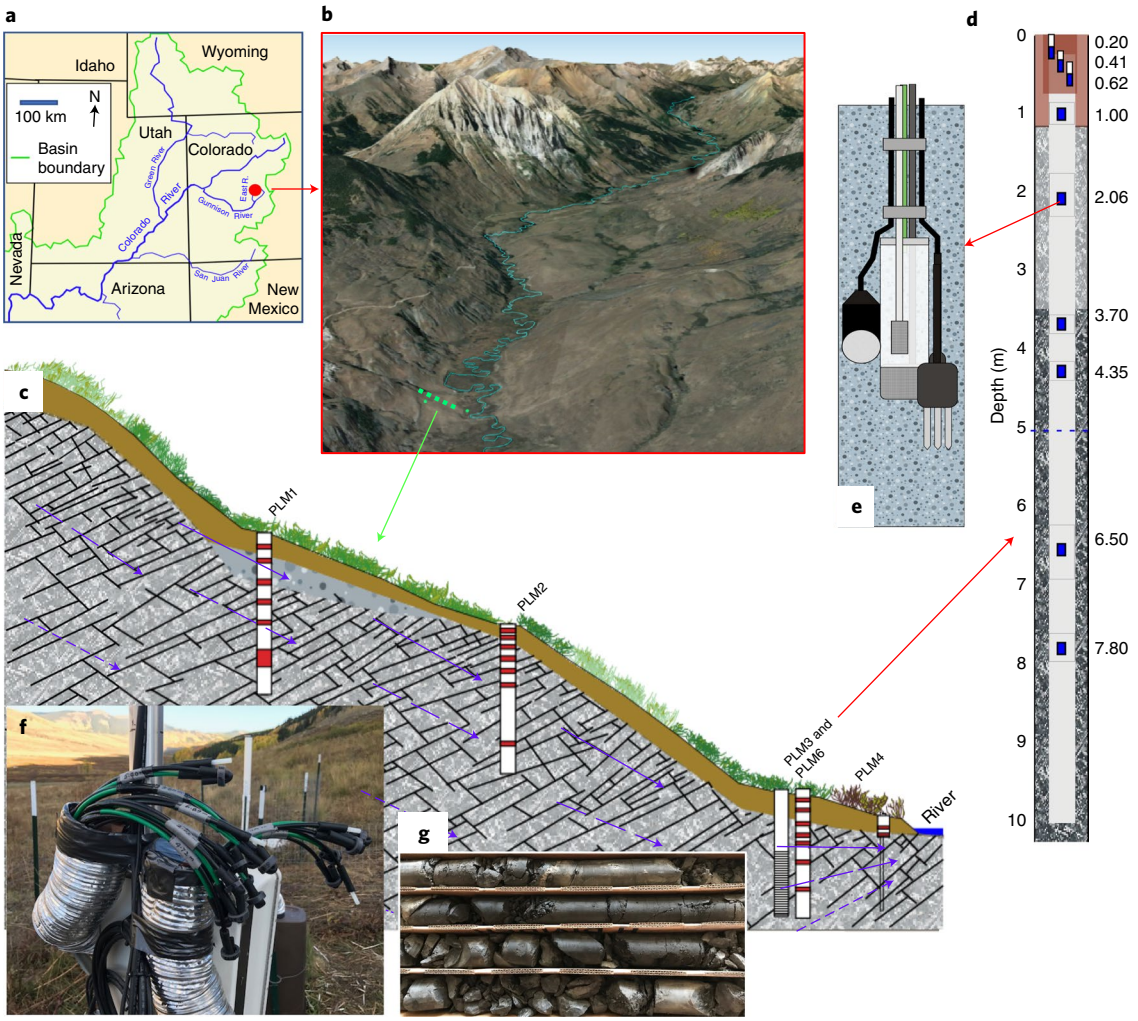

Fig. 1 | The East River watershed study site and instrumentation. a, Colorado River Basin, with location of upper East River watershed indicated by a red dot. **b**, Google Earth view northward up the East River, showing location of the lower montane hillslope transect (green dotted line). **c**, Hillslope-to-floodplain transect showing five borehole locations. PLM3 and PLM6 are at the same elevation and 5 m apart, located near the toe slope. PLM4 is located at the edge of the floodplain. Three boreholes PLM1, PLM2 and PLM3 were instrumented for long-term porewater and pore-gas sampling, and hydraulic measurements. **d**, Example of borehole cross-section showing instrumentation depths. **e**, Sensor/sampler units installed at selected depths consisting of a porewater sampler, moisture content sensor, thermistor, matric potential sensor and gas sampler. **f**, Porewater and gas sampler access tubes. **g**, Rock cores (the soil samples were hand-augered).

and PLM3, respectively (Fig. 2a). The measured annual water table depths at these locations over three years (Fig. 2b) show that the greatest depth to water table at each location matches the depth of the weathering front determined by the mineral relative concentration profiles (Fig. 2a), and that the vertical range of water table fluctuation defines the weathering zone (WZ). Products of shale pyrite and carbonate dissolution (SO_4^{2-}, H^+, Ca^{2+} and Mg^{2+}) are clearly enriched in WZ porewaters relative to that in overlying soil and underlying fractured bedrock (Fig. 2c), consistent with the relative mineral concentration profiles. Optimal oxygen and moisture conditions for rapid chemical weathering occur in the fluctuating water table zone, hence delineated the WZ. Below the deepest water table elevation, oxygen diffusion is limited relative to the rapid microbial utilization of oxygen[27]. Within the soil, the weathering reactive minerals, pyrite and carbonates, are depleted. Although hydrological controls on weathering have been recognized previously[36–38], by coupling hydrological and geochemical field measurements, we can now use seasonally fluctuating water table depths to predict subsurface weathering depths.

Subsurface reactive-N is mainly from rock weathering

Total nitrogen (TN) inventories in solid-phase soil/bedrock at three locations along the hillslope are shown in Fig. 3a. The soil contains high TN, largely as organic-N in soil organic matter, and its concentrations rapidly decrease with depth, reaching the rock-N concentration at approximately 1.0 m bgs. The unweathered shale bedrock contains $0.13 \pm 0.032\%$ N, within the range found in slates, shales and siltstones[7,39], equivalent to 32 Mg N ha^{-1} per 1.0 m thickness, a substantial source for N reentry into the terrestrial cycle through weathering. N species concentration profiles released from a laboratory water leaching experiment (Fig. 3b) reflect immediately mobile N inventories, uninfluenced by field biogeochemical processes. These data provide several important insights: (1) In soil leachates, the dominant N species is dissolved organic-N (DON). (2) Rock leachates contain primarily NH_4^+ and DON, indicating the importance of inorganic-N (NH_4^+) released from clay minerals[11]. (3) Extractable NO_3^- concentrations are negligible in soil and rock leachates. (4) The overall extractable total dissolved-N (TDN) concentrations in the shallower WZ (1.0 to 3.0 m bgs) are

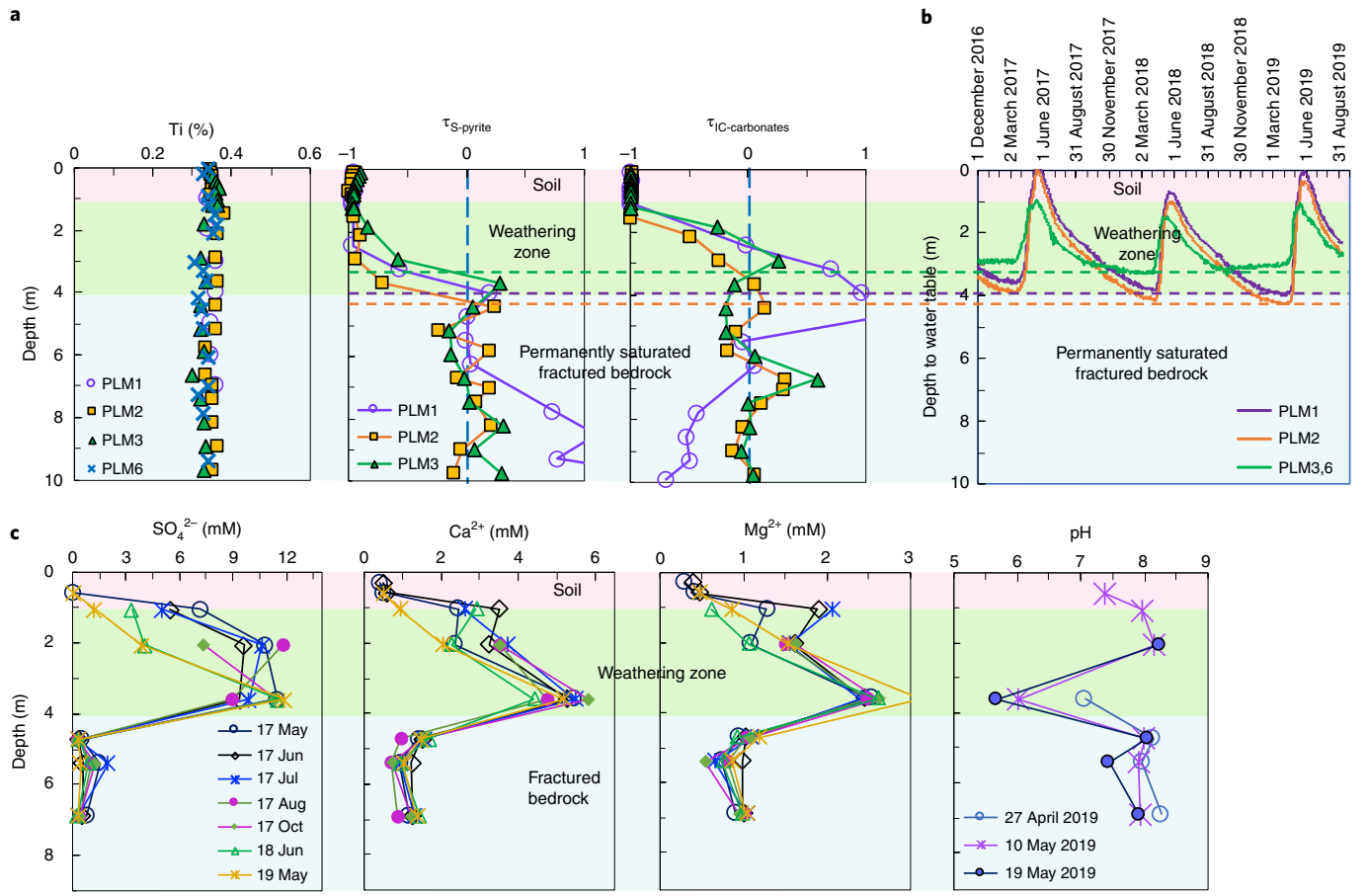

Fig. 2 | Rock weathering occurs primarily below soil, within the depth zone of the annually oscillating water table. a, Relative concentration–depth profiles of S-pyrite and IC-carbonate (uncertainties in τ are ≤0.09). Titanium (analytical uncertainty 0.04%) served as the unremovable reference element in calculations. At $\tau_j = -1$, a mineral is completely depleted, and the depth crossing $\tau_j = 0$ (vertical dashed line) is used to identify weathering fronts. **b**, Time-dependent water table depths measured over the course of three years (depth uncertainties ≤0.05 m). The lowest water table depths (marked by horizontal dashed lines) match the depths of the weathering fronts determined by relative concentration–depth profiles (Fig. 2a). **c**, Depth profiles of dissolved species from the most weathering-diagnostic minerals pyrite and carbonates and pH (note that the pH values were measured in spring 2019 only) in field porewaters from PLM1. Relative uncertainties in concentrations are ≤0.03.

depressed, reflecting depletion of N within the WZ. Figure 3c shows N species concentration profiles in field porewaters collected over the course of three years. When compared with the laboratory leachates, these data reveal new understandings into subsurface weathering and N behaviour. First, the TDN concentrations are several-fold higher in the WZ porewaters than in the overlying soil and underlying bedrock, indicating that the TDN is largely sourced from rock weathering. Secondly, NO_3^- is the dominant N species within WZ porewaters, and is only present at high concentrations in the WZ, despite occurring at negligible concentrations in laboratory extracts of soil and rock, indicating significant nitrification of weathering-released NH_4^+ and DON. Mixing of soil and WZ porewaters occurs during snowmelt displacement of soil water into the WZ, and during water table rise of N-rich WZ porewaters into the soil. Low NO_3^- concentrations in the deepest WZ and bedrock porewaters are consistent with denitrification in these reducing zones. Pore-gas samples collected from soil and the WZ from May 2017 to May 2020 (Fig. 3d) show that nitrous oxide (N_2O) concentrations span three orders of magnitude, ranging from atmospheric concentrations (0.33 ppm) to over 200 ppm. These unique subsurface depth- and time-resolved N species measurements provided part of the basis for calculating rates of N release and exports. The remaining necessary information requires the quantification of rates of subsurface water flow and gas diffusion.

Rates of weathering, N release and N-exports

Time-dependent fluxes of porewaters along the bedrock, WZ and soil layers are needed to determine rates of hillslope bedrock weathering and dissolved-N export. Briefly, calculations of subsurface flow applied the transmissivity feedback method[40] to the three-layer (soil, WZ and fractured bedrock) system, with water mass balance constrained by annual precipitation minus evapotranspiration. To constrain predictions of subsurface flow and transport, these calculations were applied to two scenarios: one based on field-measured hydraulic conductivities, K, in each zone, and the other using amplified K values. Water mass conservation set the upper limit for amplified K in the soil and WZ to 25 and 1.5 times their measured values, respectively. The resulting calculated fluxes through the three subsurface zones and their dependence on water table depth are presented in Fig. 4a1. The results based on measured and enhanced K are represented by thin and thick curves, respectively.

Weathering was quantified as the annual export per unit watershed area of the sum of base cation equivalents (BC = Na + 2Mg + K + 2Ca)[27,41], using a correlation between specific conductance (SC) and BC (Methods and Extended Data Fig. 1). Measured SC trends (Fig. 4a2) show distinctions between the soil, WZ and fractured bedrock zone, with the highest SC occurring within the WZ. By multiplying daily subsurface flow rates in each zone (Fig. 4a1) by their associated BC concentration (represented

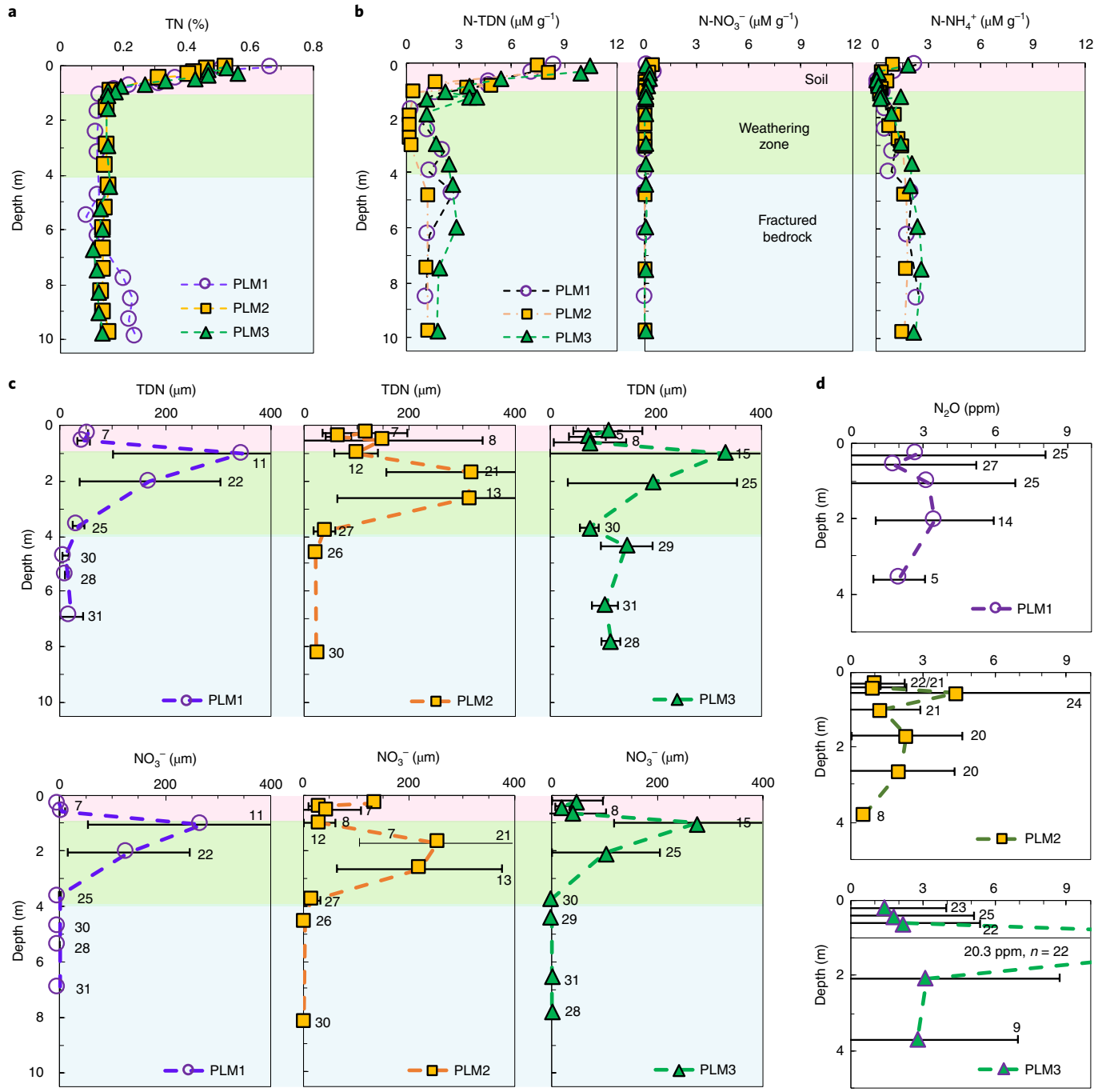

Fig. 3 | The hillslope subsurface reactive-N is primarily from bedrock weathering, not from soil. a, Total nitrogen (TN) in soil/bedrock. The unweathered shale bedrock contains 0.13 ± 0.032% N (excluding a hot spot). Relative uncertainties in individual values are ≤0.03. **b**, N species concentrations released from soil and rock through laboratory water leaching. Relative uncertainties in individual values are ≤0.03. **c**, N species concentration–depth profiles in field porewaters (averages of all samples, with the numbers of samples presented at each depth). Low matric potentials often prevented porewater collection in soil and WZ. NO_3^- appears in WZ porewaters only, showing that nitrification and mineralization transform the rock- and soil-released NH_4^+ and DON to NO_3^-. The fractured bedrock at PLM3, being located at the toe slope, receives some WZ porewaters from upslope regions. **d**, Depth-resolved N_2O concentrations in pore-gas samples show elevated N_2O in nearly all the samples relative to the atmospheric concentration of approximately 0.33 ppm. Horizontal bars span ranges of measured values.

by SC in Fig. 4a2), daily BC export rates are obtained (Fig. 4a3). Because BC export rates are highest within the WZ, only exports from this zone and the total subsurface exports are shown, by the green and blue trend lines, respectively. As before, the results based on measured and enhanced *K* are represented by thin and thick curves, respectively. Export rates increase during water table rise not only because the transmissive saturated zone becomes thicker but also because flow mobilizes the solute-rich WZ porewaters. The BC export rates averaged from water year (WY) 2017 through WY2019 are 53.1 and 57.5 $kmol_c$ ha^{-1} $year^{-1}$, for calculations based on the measured and enhanced *K* profiles, respectively. The average of these two scenarios and their differences are taken as the best-estimate BC export rate and uncertainty, respectively, 55.3 ± 4.4 $kmol_c$ ha^{-1} $year^{-1}$.

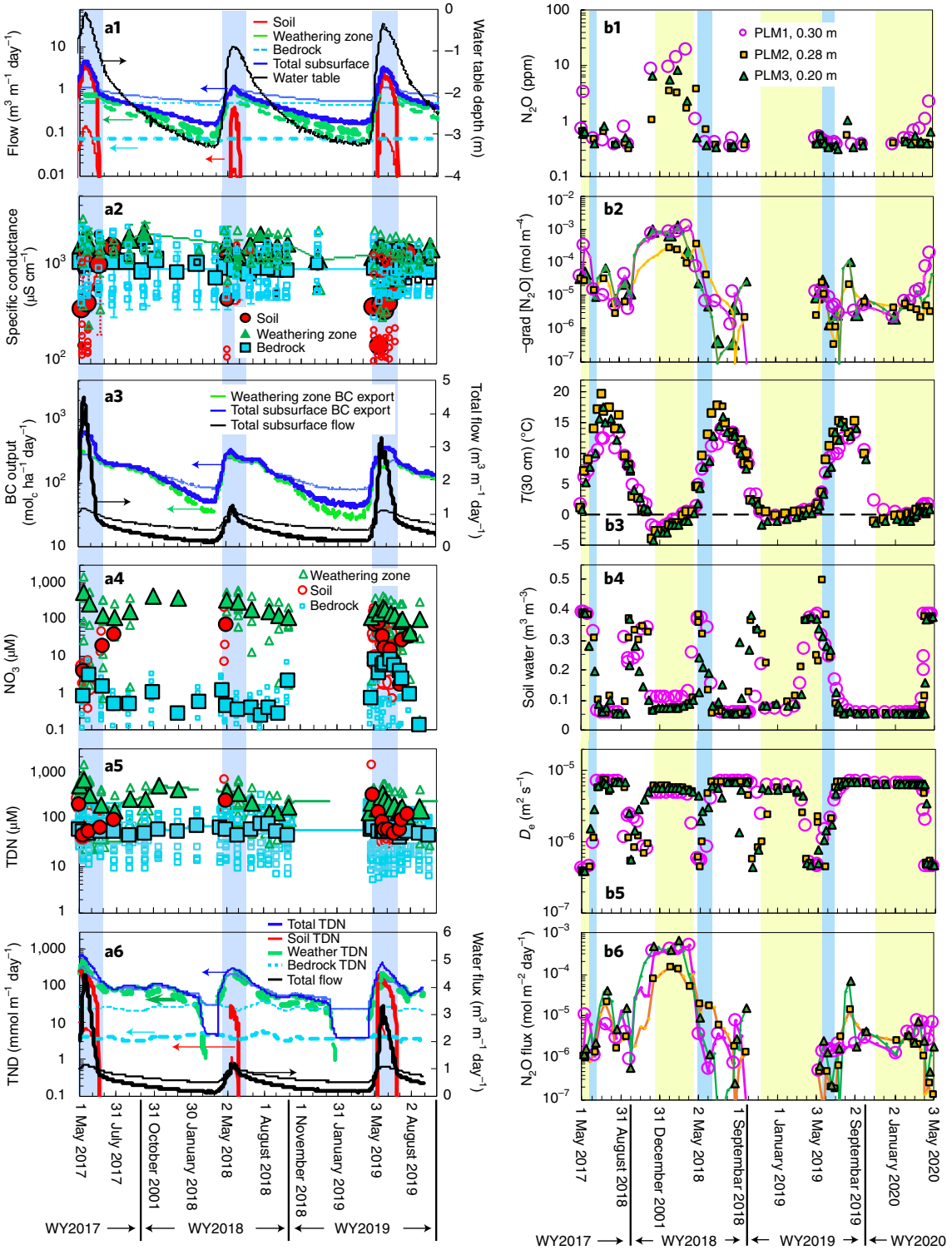

Fig. 4 | Measurements and rate calculations of bedrock weathering, dissolved-N export to hydrosphere and N_2O to atmosphere. a1, Time- and depth-dependent downslope water fluxes in three zones using measured and amplified hydraulic conductivity (*K*). Here and elsewhere, results based on measured and enhanced *K* are indicated by light and heavy curves, respectively, and constrain uncertainties in flow and transport rates. Arrows on curves point to associated axes. **a2**, Time- and depth-dependent specific conductance (SC) in the three zone porewaters. Larger symbols represent averages, and vertical bars indicate standard errors. **a3**, Time- and depth-resolved total subsurface flow rates, and rates of base cation (BC) discharge for the WZ and total subsurface. **a4**, Temporal variation of NO_3^-. **a5**, Temporal variation of TDN within the three strata (relative standard deviations ≤0.03). The trend lines are fitted through the average values. **a6**, TDN discharge fluxes within each subsurface zone obtained by multiplying porewater TDN trends by their respective Darcy fluxes. The light-blue shaded segments denote 2-month intervals with maximum subsurface flow and TDN discharge rates during each year. **b1**, Time trends of soil gas N_2O concentrations within the surface soil (relative uncertainties ≤0.05). **b2**, N_2O concentration gradient. **b3**, Soil temperature (uncertainties ≤1 °C). **b4**, Volumetric water content (uncertainties ≤0.03). **b5**, Effective N_2O diffusion coefficient (relative uncertainties ≤0.15). **b6**, Diffusive N_2O efflux to the atmosphere (relative uncertainties ≤0.2). Blue and yellow backgrounds indicate periods with highest water table positions and with snow cover, respectively.

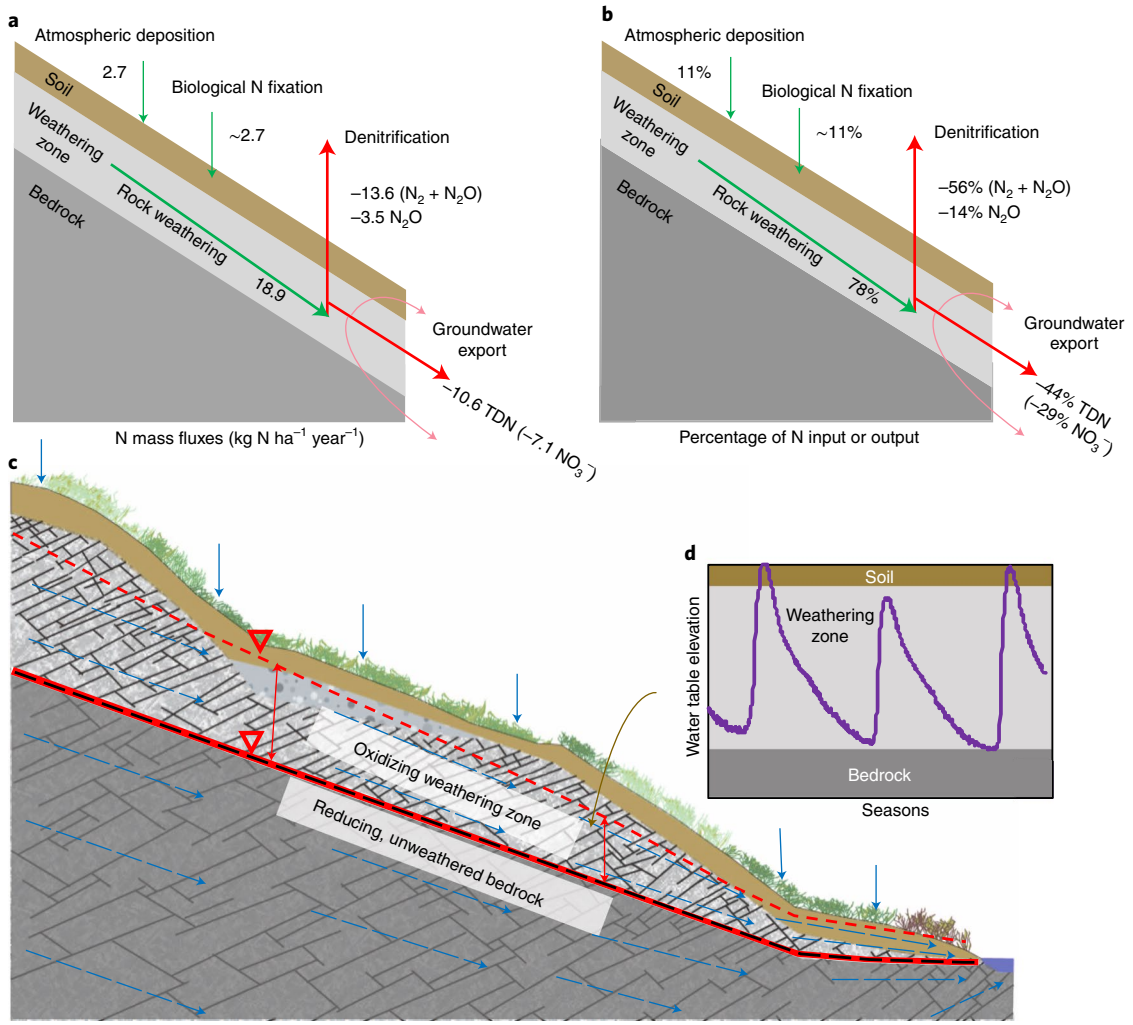

Fig. 5 | Conceptual model for hillslope bedrock-N weathering release and exports with N mass balance. a,**b**, Hillslope N mass fluxes (**a**) and percentage of N input/output (**b**), indicating that the influx rates from bedrock-N release are over three times greater than that of the combined atmospheric deposition and BNF. About 77 ± 14% of the TDN export from the hillslope subsurface to the floodplain occurs along the WZ, with 44 ± 5% of it occurring during the two-month period of maximum snowmelt-driven flow. Denitrification losses account for about 56% of the total subsurface reactive-N, with more than a quarter of it attributable to N_2O. **c**,**d**, Weathering is controlled by water table depth, within the fluctuating water table zone, where the optimal oxygen and moisture conditions promote rapid biogeochemical reactions.

Following similar rock mass balance analyses[9,39], the measured BC weathering rate of 55.3 ± 4.4 $kmol_c$ ha^{-1} $year^{-1}$ was scaled with the measured shale bedrock-N:BC ratio = 0.0244 mol mol_c^{-1}, resulting in a rock-N release rate of 18.9 ± 4.6 kg N ha^{-1} $year^{-1}$. This rock-N release rate is greater than most literature values[20,42], indicating the importance of chemical weathering of N-rich sedimentary rocks. Comparing this rock-N influx with inputs from atmospheric deposition and estimated BNF (2.68 kg N ha^{-1} each), we find that 78% of the hillslope reactive-N originates from bedrock weathering. This quantification of N influxes shows the overwhelming importance of reactive-N released through bedrock weathering at this hillslope underlain by weathering marine shale.

Advective transport of dissolved-N was calculated as the product of time-dependent Darcy fluxes and N concentrations within each zone. Temporal variations of NO_3^- and TDN concentrations in Fig. 4a4,a5 show their highest concentrations occurring in the WZ. Curves fitted through average TDN values within each zone (Fig. 4a5) were multiplied by their respective Darcy fluxes (Fig. 4a1) to obtain the rates of TDN discharge in Fig. 4a6 (Methods). Annual two-month periods with maximum snowmelt-driven transport are highlighted with blue backgrounds in Fig. 4a1–6 to emphasize the strong seasonality of subsurface TDN export rates. These annual 'hot moments' account for about 44% (±5%) of TDN exports. Per unit width of the transect, average exports under the different *K* scenarios amount to 33 and 41 mol TDN m^{-1} $year^{-1}$, equivalent to export rates of 9.5 and 11.8 kg of N ha^{-1} $year^{-1}$, respectively. Thus, the representative TDN export rate is 10.6 ± 1.2 kg N ha^{-1} $year^{-1}$ (Extended Data Fig. 1).

Rates of N loss by denitrification from the hillslope can be calculated from the difference between N inputs (bedrock weathering and atmospheric sources including BNF) and N-outputs[13]. The denitrification rate calculated by subtracting porewater TDN exports from the sum of inputs is 13.6 ± 0.8 kg N ha^{-1} $year^{-1}$, slightly greater than the sum of estimated global average watershed soil and groundwater denitrification rates, 12.04 kg N ha^{-1} $year^{-1}$ (ref. [43]). Hillslope denitrification losses amount to 56% of the hillslope reactive-N inputs, 10% higher than the calculated global soil average of 46% (ref. [43]). These denitrification rates obtained by subtracting outputs from inputs in order to close the hillslope N mass balance warrant comparisons with independent diffusion

calculations. While N_2 is expected to be the dominant product of denitrification, its high atmospheric concentrations make the efflux from the subsurface difficult to quantify. In contrast, the low natural abundance of N_2O in the atmosphere facilitates calculations of its diffusive export (Methods). Figure 4b1 shows time trends in N_2O concentrations collected from the shallow soil depths at the three hillslope locations, which permit calculation of diffusion gradients driving N_2O to the atmosphere (Fig. 4b2). The seasonal variations in shallow soil temperature (Fig. 4b3) and volumetric water content (Fig. 4b4) give rise to variations in the effective diffusion coefficient D_e for N_2O within the surface soils (Fig. 4b5). Time trends for N_2O effluxes to the atmosphere (Fig. 4b6) were obtained from the product of D_e and concentration gradients[44]. The highest N_2O effluxes at all three locations occurred in winter 2017–2018, a perplexing 'hot moment'[2]. The calculated N_2O flux rates (2017–2020) from the three locations amount to 5.9 ± 3.2 and 0.99 ± 0.75 kg N ha^{-1} year^{-1}, with and without the 'hot moment', respectively, constituting 44% and 7% of the hillslope denitrification. The average and range of these values, 25 ± 18%, fall within the very wide range (77% to 1%, average 20.7%) reported in a synthesis of studies of natural ecosystems. The overall hillslope N fluxes and mass balance are presented in Extended Data Fig. 3.

Rock-N weathering release and implications

By integrating subsurface hydrological and biogeochemical measurements, quantitative understanding of the hillslope N cycle becomes possible (Fig. 5). Bedrock weathering occurs primarily within the zone of annual water table oscillation that we defined as the WZ. At this site, about 78% of the total subsurface reactive-N is sourced from the WZ, contrary to the common belief that atmospheric sources are the sole N sources in pristine environments. High concentrations of nitrate accumulate in WZ porewaters, mostly from nitrification of bedrock-derived NH_4^+ and DON. Thus, the widely observed NO_3^- accumulation in the vadose zone that is generally attributed to fertilization and soil leaching[45] can also reflect subsurface weathering in regions where N-containing bedrock is under favourable oxidizing and moisture conditions[11].

The importance of bedrock-N contributions to global N_2O emissions becomes evident upon inspection of global N fluxes. About 10–18 Tg rock-N year^{-1} is released globally[9,31]. Applying our measured 56% denitrification of reactive-N with 25% of denitrification lost as N_2O, this extrapolates to 1.4–2.5 Tg N-N_2O year^{-1} sourced from bedrock weathering globally. A similar range of 1.0–1.7 Tg N-N_2O year^{-1} is obtained solely from literature review values of terrestrial N fluxes, using 46% denitrification[43] and 21% of denitrified N lost as N_2O. The latter value was taken from a review that summarized results from nine natural field sites. Our determination that 25% of denitrified N is lost as N_2O is well within one standard error of the average (20.7 ± 7.9%) reported in this review. Thus, our study is consistent with others' results, and provides a framework for investigations into the fate of rock-N in other settings. The underlying assumptions are that rock-N releases can be quantified by combining measured rock weathering profiles with export calculations of dissolved-N and gaseous N_2O. Uncertainties associated with the aqueous fluxes were constrained with upper and lower estimates of porewater velocities, while the gaseous flux uncertainty was constrained by including and excluding an apparent N_2O hot-moment efflux. Both our study and calculations based solely on literature values suggest that the global terrestrial N-N_2O flux (10.0 ± 2.0 Tg N-N_2O year^{-1})[5] includes a significant and previously unrecognized contribution of roughly 10–20% from bedrock weathering.

Online content

Any methods, additional references, Nature Research reporting summaries, source data, extended data, supplementary information, acknowledgements, peer review information; details of author contributions and competing interests; and statements of data and code availability are available at https://doi.org/10.1038/s41561-021-00717-0.

Received: 17 July 2020; Accepted: 22 February 2021;
Published online: 5 April 2021

References

1. Bremner, J. M. Sources of nitrous oxide in soils. *Nutr. Cycl. Agroecosystems* **49**, 7–16 (1997).
2. Bouwman, A. F. et al. Global trends and uncertainties in terrestrial denitrification and N_2O emissions. *Philos. Trans. R. Soc. B* **368**, https://doi.org/10.1098/rstb.2013.0112 (2013).
3. Ravishankara, A. R., Daniel, J. S. & Portmann, R. W. Nitrous oxide (N_2O): the dominant ozone-depleting substance emitted in the 21st century. *Science* **326**, 123–125 (2009).
4. Thompson, R. L. et al. Acceleration of global N_2O emissions seen from two decades of atmospheric inversion. *Nat. Clim. Change* **9**, 993 (2019).
5. Tian, H. Q. et al. Global soil nitrous oxide emissions since the preindustrial era estimated by an ensemble of terrestrial biosphere models: magnitude, attribution, and uncertainty. *Global Change Biol.* **25**, 640–659 (2019).
6. Butterbach-Bahl, K., Baggs, E. M., Dannenmann, M., Kiese, R. & Zechmeister-Boltenstern, S. Nitrous oxide emissions from soils: how well do we understand the processes and their controls? *Philos. Trans. R. Soc. B* **368**, 1621 (2013).
7. Johnson, B. & Goldblatt, C. The nitrogen budget of Earth. *Earth Sci. Rev.* **148**, 150–173 (2015).
8. Holloway, J. M. & Dahlgren, R. A. Nitrogen in rock: occurrences and biogeochemical implications. *Global Biogeochem. Cycles* **16**, https://doi.org/10.1029/2002gb001862 (2002).
9. Houlton, B. Z., Morford, S. L. & Dahlgren, R. A. Convergent evidence for widespread rock nitrogen sources in Earth's surface environment. *Science* **360**, 58–62 (2018).
10. Morford, S. L., Houlton, B. Z. & Dahlgren, R. A. Direct quantification of long-term rock nitrogen inputs to temperate forest ecosystems. *Ecology* **97**, 54–64 (2016).
11. Sullivan, P. J., Sposito, G., Strathouse, S. M. & Hansen, C. L. Geologic nitrogen and the occurrence of high nitrate soils in the western San-Joaquin Valley, California. *Hilgardia* **47**, 15–49 (1979).
12. Butterbach-Bahl, K. et al. in *The European Nitrogen Assessment* (eds M. A. Sutton et al.) Ch. 6 (Cambridge Univ. Press, 2011).
13. Van Breemen, N. et al. Where did all the nitrogen go? Fate of nitrogen inputs to large watersheds in the northeastern USA. *Biogeochemistry* **57**, 267–293 (2002).
14. Williams, L. B., Wilcoxon, B. R., Ferrell, R. E. & Sassen, R. Diagenesis of ammonium during hydrocarbon maturation and migration, Wilcox-Group, Louisiana, USA. *Appl. Geochem.* **7**, 123–134 (1992).
15. Muller, P. J. C/N ratios in Pacific deep-sea sediments: effect of inorganic ammonium and organic nitrogen compounds sorbed by clays. *Geochim. Cosmochim. Acta* **41**, 765–776 (1977).
16. Morrison, S. J., Goodknight, C. S., Tigar, A. D., Bush, R. P. & Gil, A. Naturally occurring contamination in the Mancos Shale. *Environ. Sci. Technol.* **46**, 1379–1387 (2012).
17. Tuttle, M. L. W., Fahy, J. W., Elliott, J. G., Grauch, R. I. & Stillings, L. L. Contaminants from Cretaceous black shale: II. Effect of geology, weathering, climate, and land use on salinity and selenium cycling, Mancos Shale landscapes, southwestern United States. *Appl. Geochem.* **46**, 72–84 (2014).
18. Riebe, C. S., Kirchner, J. W. & Finkel, R. C. Long-term rates of chemical weathering and physical erosion from cosmogenic nuclides and geochemical mass balance. *Geochim. Cosmochim. Acta* **67**, 4411–4427 (2003).
19. Montgomery, D. R. & Brandon, M. T. Topographic controls on erosion rates in tectonically active mountain ranges. *Earth Planet. Sci. Lett.* **201**, 481–489 (2002).
20. Morford, S. L., Houlton, B. Z. & Dahlgren, R. A. Geochemical and tectonic uplift controls on rock nitrogen inputs across terrestrial ecosystems. *Global Biogeochem. Cycles* **30**, 333–349 (2016).
21. West, A. J., Galy, A. & Bickle, M. Tectonic and climatic controls on silicate weathering. *Earth Planet. Sci. Lett.* **235**, 211–228 (2005).
22. Holloway, J. M. & Smith, R. L. Nitrogen and carbon flow from rock to water: regulation through soil biogeochemical processes, Mokelumne River watershed, California, and Grand Valley, Colorado. *J. Geophys. Res. Earth* **110**, F01010 (2005).
23. Hubbard, S. S. et al. The East River, Colorado, watershed: a mountainous community testbed for improving predictive understanding of multiscale hydrological-biogeochemical dynamics. *Vadose Zone J.* **17**, 180061 (2018).
24. Gaskill, D. L., Mutschler, F. E., Kramer, J. H., Thomas, J. A. & Zahoney, S. G. *Geologic Map of the Gothic Quadrangle, Colorado, Gunnison County, Department of Interior* (USGS, 1991).

25. Carroll, R. W. H. et al. Factors controlling seasonal groundwater and solute flux from snow-dominated basins. *Hydrol. Process.* **32**, 2187–2202 (2017).
26. Winnick, M. J. et al. Snowmelt controls on concentration-discharge relationships and the balance of oxidative and acid–base weathering fluxes in an alpine catchment, East River, Colorado. *Water Resour. Res.* **53**, 2507–2523 (2017).
27. Wan, J. M. et al. Predicting sedimentary bedrock subsurface weathering fronts and weathering rates. *Sci. Rep.* **9**, https://doi.org/10.1038/s41598-019-53205-2 (2019).
28. Tokunaga, T. K. et al. Depth- and time-resolved distributions of snowmelt-driven hillslope subsurface flow and transport and their contributions to surface waters. *Water Resour. Res.* **55**, 9474–9499 (2019).
29. *CASTNET* (US Environmental Protection Agency, 2019).
30. Darrouzet-Nardi, A., Erbland, J., Bowman, W. D., Savarino, J. & Williams, M. W. Landscape-level nitrogen import and export in an ecosystem with complex terrain, Colorado Front Range. *Biogeochemistry* **109**, 271–285 (2012).
31. Vitousek, P. M., Menge, D. N. L., Reed, S. C. & Cleveland, C. C. Biological nitrogen fixation: rates, patterns and ecological controls in terrestrial ecosystems. *Philos. Trans. R. Soc. B* **368**, https://doi.org/10.1098/rstb.2013.0119 (2013).
32. Anderson, S. P., Dietrich, W. E. & Brimhall, G. H. Weathering profiles, mass-balance analysis, and rates of solute loss: linkages between weathering and erosion in a small, steep catchment. *Geol. Soc. Am. Bull.* **114**, 1143–1158 (2002).
33. Brimhall, G. H. & Dietrich, W. E. Constitutive mass balance relations between chemical-composition, volume, density, porosity, and strain in metasomatic hydrochemical systems – results on weathering and pedogenesis. *Geochim. Cosmochim. Acta* **51**, 567–587 (1987).
34. Littke, R., Klussmann, U., Krooss, B. & Leythaeuser, D. Quantification of loss of calcite, pyrite, and organic-matter due to weathering of toarcian black shales and effects on kerogen and bitumen characteristics. *Geochim. Cosmochim. Acta* **55**, 3369–3378 (1991).
35. Galy, A. & France-Lanord, C. Weathering processes in the Ganges–Brahmaputra Basin and the riverine alkalinity budget. *Chem. Geol.* **159**, 31–60 (1999).
36. Brantley, S. L. et al. Toward a conceptual model relating chemical reaction fronts to water flow paths in hills. *Geomorphology* **277**, 100–117 (2017).
37. Manning, A. H., Verplanck, P. L., Caine, J. S. & Todd, A. S. Links between climate change, water-table depth, and water chemistry in a mineralized mountain watershed. *Appl. Geochem.* **37**, 64–78 (2013).
38. Torres, M. A., West, A. J. & Clark, K. E. Geomorphic regime modulates hydrologic control of chemical weathering in the Andes–Amazon. *Geochim. Cosmochim. Acta* **166**, 105–128 (2015).
39. Holloway, J. M. & Dahlgren, R. A. Geologic nitrogen in terrestrial biogeochemical cycling. *Geology* **27**, 567–570 (1999).
40. Rodhe, A. On the generation of stream runoff in till soils. *Nord Hydrol* **20**, 1–8 (1989).
41. Horton, T. W., Chamberlain, C. P., Fantle, M. & Blum, J. D. Chemical weathering and lithologic controls of water chemistry in a high-elevation river system: Clark's Fork of the Yellowstone River, Wyoming and Montana. *Water Resour. Res.* **35**, 1643–1655 (1999).
42. Holloway, J. M., Dahlgren, R. A., Hansen, B. & Casey, W. H. Contribution of bedrock nitrogen to high nitrate concentrations in stream water. *Nature* **395**, 785–788 (1998).
43. Seitzinger, S. et al. Denitrification across landscapes and waterscapes: a synthesis. *Ecol. Appl.* **16**, 2064–2090 (2006).
44. Tokunaga, T. K. et al. Deep vadose zone respiration contributions to carbon dioxide fluxes from a semiarid floodplain. *Vadose Zone J.* **15**, https://doi.org/10.2136/vzj2016.02.0014 (2016).
45. Ascott, M. J. et al. Global patterns of nitrate storage in the vadose zone. *Nat. Commun.* **8**, 1416 (2017).

Publisher's note Springer Nature remains neutral with regard to jurisdictional claims in published maps and institutional affiliations.

© The Author(s), under exclusive licence to Springer Nature Limited 2021

Methods

Study site. The study site[23] is situated in the upper East River Basin, a headwater mountainous watershed situated in the Upper Colorado River Basin (Fig. 1a). The watershed has an average elevation of 3,266 m, with 1,420 m of topographic relief. The area has a continental, subarctic climate with long cold winters, short cool summers, a mean annual temperature of 3 °C and mean annual precipitation of about 680 mm (approximately 70% as snow). Excursions in river discharge are driven primarily by snowmelt in spring to early summer. This study was conducted along a northeast-facing hillslope transect (Fig. 1b) that adjoins a riparian floodplain along the East River, which in turn drains into the Gunnison River, a major tributary of the Colorado River. The hillslope is vegetated with grasses, forbs and shrubs representative of regional lower montane meadow environments, and the majority of roots are shallower than 20 cm and seldom deeper than 1.0 m. The hillslope is underlain by Mancos Shale.

Field drilling, instrumentation and hydraulic measurements. Along the hillslope-to-floodplain flow transect (Fig. 1c), we drilled five 10-m-deep boreholes (0.14 m diameter) into the bedrock along a 137-m-long hillslope transect, including one borehole in the floodplain. We collected solid samples over the soil-to-bedrock continuum, and installed instruments (moisture sensors, porewater samplers and gas samplers) at different depths inside the boreholes for long-term hydrologic monitoring and geochemical sampling (Fig. 1d–g). Locations PLM1, PLM2 and PLM3 on the hillslope were instrumented for depth-resolved measurements to as deep as 8.2 m bgs. Note that location PLM3 is at the toe slope, and the mid-slope location PLM2 is elevated by about 2 m relative to the average hillslope profile. At the floodplain location PLM4, samplers and instruments were installed to a maximum depth of only 1.28 m because the original borehole collapsed prior to instrument installation. Location PLM6, located 4.5 m away from PLM3 at the same elevation, was drilled to recover continuous core samples and to install a groundwater monitoring well; it did not contain depth-distributed instrumentation. The water table depth below the local soil surface at PLM1 and PLM6 was recorded continuously using pressure transducers (AquaTROLL 200). At all of the other PLM locations, water table depths were determined from equilibrium pressure measurements in porewater samplers using the 'tensisampler' method and from depth-distributed moisture sensors. At PLM4, depths to the water table were also obtained from the correlation between locally measured groundwater levels and continuously measured East River water levels.

Soil and rock sampling and analyses. Soil thickness along the hillslope was measured by hand-auger (0.07 m diameter) in 0.10 m depth increments down to as deep as the auger could be advanced. The soil thickness is defined as the depth at which manual core sampling was no longer possible (meets the rock). Based on 40 hand-cored soil samples, the soil depths are 0.9–1.1 m, 0.7–0.9 m and 1.0–1.3 m bgs at stations PLM1, PLM2 and PLM3, respectively. Thus, the soil depths on this hillslope are approximately 1.0 ± 0.3 m bgs. At PLM4, the soil depth is 0.7–0.8 m bgs. These hand-augered soil samples were later used for chemical and mineral analyses. Roots, only found in the shallow soil samples above about 20 cm, were removed before further sample processing. Deeper than approximately 1 m bgs, rock samples were collected in 0.6–0.7 m depth increments from boreholes at locations PLM1–4 and PLM6. The soil and rock samples were oven-dried at 75 °C for 3 days, then milled to grain sizes less than about 50 µm for subsequent analyses. Solid-phase elemental compositions were determined using X-ray fluorescence (XRF) by the Geochemistry Division of the commercial laboratory ALS Global (http://www.alsglobal.com/geochemistry), with analytical uncertainty <0.1% based on three replicate measurements. Mineralogical analyses were conducted using quantitative X-ray diffraction (XRD) by the commercial laboratory Xrayminerals (http://www.xrayminerals.co.uk), with relative uncertainties <10%. Total nitrogen contents were determined using elemental analyses (EA) by the Isotope Core Laboratory at Washington State University (https://www.isotopes.wsu.edu), with relative uncertainties <3%. Inorganic carbon (IC) and organic carbon (OC) were determined using a Shimadzu TOC-VCSH carbon analyser by our own Lawrence Berkeley National Laboratory/Earth and Environment Sciences Area aqueous geochemistry laboratory with relative uncertainty <1%.

Relative concentrations $\tau_{i,j}$ of weathering profile elements[32,33] were defined by

$$\tau_{i,j} = \frac{C_{j,w} C_{i,p}}{C_{j,p} C_{i,w}} - 1 \quad (1)$$

where C is concentration, the subscript j represents a mobile constituent (element or mineral of interest) and the subscript i represents the immobile reference element titanium (Ti) associated with the parent rock. Subscripts 'w' and 'p' denote weathered and parent rock, respectively. The concentrations of element/mineral j and i in parent rock were determined by averaging their respective parent rock concentrations.

Fluid-phase sampling and analyses. The water leachates of soil-rock samples were obtained using an artificial groundwater recipe of 5 mM $CaCl_2$ and 5 mM NaCl in equilibrium with atmospheric CO_2. The solid-to-water ratio is 1:10. The soil-rock solid samples were powdered to about 50 µM. After 24 h of slow mixing on a reciprocating shaker, the aqueous phase was separated by centrifugation and filtration (0.45 µm). The NH_4^+ concentration was analysed immediately, then the TDN and NO_3 concentrations, using the analytic methods described below.

Porewater was collected from depth-distributed lysimeters at about monthly intervals from fall 2016 to winter 2019, and approximately three times per month in spring to summer in 2019. The collected porewaters were immediately filtered in the field (0.45 µm polytetrafluoroethylene syringe filters), and divided into subsamples for different types of analyses. The samples were shipped overnight to the laboratory in a cooler containing ice packs, and refrigerated or frozen for later analyses.

Porewater cation concentrations were measured using an inductively coupled plasma mass spectrometer (Thermo Fisher, MA, USA). Anions including NO_3^- and NO_2^- were measured using an ion chromatograph (Dionex ICS-2100, Thermo Scientific, USA) with precision of ±5% of reported values. Dissolved organic carbon (DOC) and inorganic carbon (DIC) were determined using a TOC-VCPH analyser (Shimadzu Corporation, Japan). DOC was analysed as non-purgeable organic carbon (NPOC) by purging acidified samples with carbon-free air to remove DIC prior to measurement. Total dissolved nitrogen (TDN) was analysed using a Shimadzu total nitrogen module (TNM-1) combined with a TOC-VCSH analyser (Shimadzu Corporation, Japan), with precision of ±3% of reported values. All nitrogen species in samples are combusted to nitrogen monoxide and nitrogen dioxide, then reacted with ozone to form an excited state of nitrogen dioxide. Upon returning to ground state, light energy is emitted and TN is measured using a chemiluminescence detector. For DOC/DIC/TDN in porewater samples, a relative standard deviation (RSD) of <3% was estimated from three to five replicates. Ammonia (NH_4^+) was determined using a Lachat's QuikChem 8500 series 2 flow injection analysis system (automated ion analyser, LACHAT Instruments). An RSD of <3% was obtained based on two replicate measurements. Pore-gas samples were collected from the depth-distributed pore-gas samplers in subsurface unsaturated regions. In the field, the gas extracted from certain depth was injected and slightly over-pressurized into 50 mL pre-evacuated serum glass vials sealed with 14-mm-thick chlorobutyl septa (Bellco Glass, Inc.). Concentrations of CO_2, N_2O and CH_4 were analysed using a Shimadzu gas chromatograph (GC-2014), with a precision of ±5% of the reported value.

Porewater flux calculations. Downslope flow of porewaters was determined based on calculations of water table elevation-dependent Darcy fluxes in the fractured bedrock, WZ and soil. Briefly, flow in each of these zones was equated with the product of its hydraulic conductivity K, its saturated thickness and the hydraulic head gradient. Subsurface water fluxes were calculated using two scenarios to constrain predictions. One scenario was based on the field-measured K in each zone, while the other used K values greater than those measured in the field, recognizing that local measurements of K commonly yield values that are too low to represent hillslope-scale flow. For the field measurements-based case, K values of the surface soil, subsoil, WZ and fractured bedrock were assigned values of 9.7×10^{-6}, 7.9×10^{-6}, 1.1×10^{-5} and 1.6×10^{-7} m s^{-1}, respectively. The saturated thicknesses of each zone were determined by continuous piezometer (pressure transducer) measurements. Piezometric measurements showed that the hydraulic head gradient remained very close to the slope of the soil surface along the transect, and the much higher K of shallower zones relative to the fractured bedrock supported application of the transmissivity feedback approach[40,46] for describing subsurface flow. Given the large uncertainties associated with K, as well as observations that K measurements obtained in small boreholes in soil are often much lower than field-scale K measurements[47], subsurface flow calculations were also performed with K values in the soil and WZ that were 25 and 1.5 times higher than their respective field-measured values. A water mass balance constraint was applied such that the total precipitation (872 mm) minus the calculated evapotranspiration (310 mm) for water year (WY) 2017 was balanced by the transmissivity-based total subsurface flow over the same period. That mass balance constraint prevented the assignment of larger amplifications to the measured WZ K because all subsurface flow would then have to be accommodated within depths shallower than 10 m bgs, contrary to field observations. The water mass balance constraint also led to setting the depth to the operationally defined impermeable boundary at the bottom of the fractured bedrock at 176 and 29.8 m bgs, for flow calculations based on the measured and enhanced K values, respectively.

Rock weathering rate calculations. From our previous study[41], weathering rates were calculated from the export of base cations (BC: Na^+, K^+, Ca^{2+} and Mg^{2+}). Although porewater specific conductance (SC, µS cm^{-1}) is presented as a function of time and depth to represent trends in overall ion concentrations in Supplementary Fig. S2, sums of actual BC equivalent charge concentrations were used in the weathering rate calculations. The linear correlation between SC and BC (the sum of Na^+, K^+, Ca^{2+} and Mg^{2+} equivalents) was determined from a representative subset of porewater samples, yielding BC (mM$_c$) = 0.0105 mM$_c$ µS^{-1} cm × SC (ref. [27]). BC weathering rates are commonly normalized per unit area of watershed. Therefore, the product of flow rate times BC concentration was normalized on a daily basis to the area of the transect and its contributing upslope region to obtain the daily BC discharge rate. Two improvements were made over the previous weathering rate calculations. First, the integrated BC weathering rates were obtained by summing over 365-day intervals. It should be noted that

the measured BC concentrations in the fractured bedrock zone were scaled by a factor of 0.608 for export calculations based on the measured K profiles because the bedrock flow is calculated to extend down to 176 m bgs. This adjustment was made because our bedrock porewaters were sampled at only 3.7–8.2 m bgs, where solute concentrations are relatively high due to the influence of the overlying WZ. The factor 0.608 is the ratio of average BC in a 60-m-deep Mancos Shale well to the average in the PLM hillslope bedrock. The 60-m-deep well is located 5.0 km upstream within the East River watershed. The second improvement consists of adding more recent measurements and now averaging over nearly three years of porewater data. The resulting BC weathering rate of 55.3 ± 4.4 kmol$_c$ ha^{-1} year^{-1} represents the average of exports based on the measured K profiles and enhanced K profiles, with the uncertainty range spanning these two K scenarios.

Rock-N weathering rate calculations. The BC weathering rates were scaled by the concentration ratio of rock-N to the BC, following similar applications of rock mass balance[9,39]. Scaling the BC weathering rates by the measured ratio of rock-N to BC of 0.0244 yielded rock-N release rates of 1.74 and 1.52 kmol N ha^{-1} year^{-1} for the measured and enhanced K scenarios, respectively. The average and difference between these two values are taken as the best estimate rock-N release rate and its uncertainty, which on a mass basis amounts to 18.9 ± 1.5 kg N ha^{-1} year^{-1}.

Total dissolved nitrogen (TDN) export rate calculations. In the transmissivity feedback approach, the daily advective transport of TDN is calculated as the product of the Darcy flux and the TDN concentration within each zone. For this purpose, TDN concentration data from the three hillslope locations were combined to obtain time trends characteristic of the soil, WZ and fractured bedrock. Specifically, the average TDN values (averages for days with three or more individual sample analyses obtained within a given zone) served as the basis for generating continuous TDN concentration curves for each zone. TDN values for unsampled days were assigned by interpolating between nearest sampled days. For the large data gap between 29 September 2018 and 22 April 2019, the average of all TDN concentration data within a given zone was applied for days in which the water table remained within the zone. Long periods during which the water table resides below the soil–WZ interface do not contribute to downslope flow along the soil zone. Thus, the average of all measured fractured bedrock TDN concentrations was applied throughout this long gap for the bedrock, while the average WZ TDN was applied from 29 September 2018 through 25 January 2019 (after which the water table declined below the WZ).

N_2O emission rate calculations. Rates of N_2O diffusion at the soil surface at three hillslope locations were calculated following a procedure previously used for determining CO_2 fluxes[44]. The N_2O concentrations measured on samples collected from the shallowest gas samplers were used with the atmospheric N_2O concentration (330 ppb) and sampler depth (0.30, 0.28 and 0.20 m, for PLM1, PLM2 and PLM3, respectively) to calculate the concentration gradient. N_2O gradients were determined on a daily basis, interpolating between measured days. For the large data gap from 23 August 2018 to 10 May 2019, the average of all measured gradients was used for each location. The effective diffusion coefficient for N_2O in soil D_e was calculated with the water-induced linear reduction model applied to Marshall's model[48],

$$D_e = D_0 \varepsilon^{2.5} \Phi^{-1} \quad (2)$$

where ε is the air-filled porosity, Φ is the total porosity and D_0 is the diffusion coefficient for N_2O in the bulk air phase. Adjustments were applied to Massman's N_2O D_0 formula[49] by using the daily average temperature recorded by the shallowest matric potential sensor (Decagon MPS6) and average local atmospheric pressure of 72.2 kPa estimated using the Boltzmann barometric equation for the average hillslope elevation of 2,776 m. Total porosities, matric potentials and volumetric water contents needed for calculating D_e were obtained from core sample measurements at adjacent locations and sensors (Decagon 5TE and MPS6), respectively. Specific values for Φ for the midplane of the shallowest interval at PLM1, PLM2 and PLM3 were assigned as 0.58, 0.59 and 0.63, respectively, based on a third-order polynomial fit to data for the depth dependence of shallow soil bulk densities and an assumed solid density of 2.65 g cm^{-3}. Volumetric water contents were calculated by combining field matric potential sensor measurements with laboratory pressure plate moisture measurements on shallow soil samples, and with field soil moisture sensors (Decagon 5TE), then subtracted from Φ to obtain ε. Fickian N_2O fluxes were calculated as the product of D_e and the N_2O concentration gradient on a daily basis.

During periods with snowpack, N_2O concentrations increase above 330 ppb at the soil–snow interface, and the interface N_2O concentration must be estimated. For negligible storage within the snowpack, the diffusive fluxes of N_2O through the surface soil and snowpack are equal

$$D_e \frac{(C_1 - C_b)}{z_1} = D_{snow} \frac{(C_b - C_0)}{z_2} \quad (3)$$

where C_1, C_b and C_0 are the N_2O concentrations in the shallowest gas sampler, at the soil–snow boundary and in the atmosphere, respectively, D_{snow} is the effective diffusion coefficient of N_2O through snow, and z_1 and z_2 are the depth of the shallowest soil gas sampler and the thickness of the snowpack, respectively. Values of D_{snow} were estimate based on the linear reduction model (Eq. 3), with ε identical to Φ_{snow}, using daily snow densities measured at the nearby snow telemetry station (Butte SNOTEL). The snowpack thicknesses z_2 were estimated from a linear regression between measurements obtained along the hillslope transect during 2017 and 2020, and thicknesses reported from the Butte SNOTEL. Values of C_b were calculated for serial, steady-state diffusion through the surface soil and snowpack as

$$C_b = \left(\frac{z_2 D_e}{z_1 D_{snow} + z_2 D_e}\right) C_1 + \left(\frac{z_1 D_{snow}}{z_1 D_{snow} + z_2 D_e}\right) C_0 \quad (4)$$

Note that the calculated diffusive fluxes are likely underestimates because wind is expected to enhance gas fluxes through snow[50].

Data availability

Data used in this paper are published on ESS-DIVE (https://doi.org/10.15485/1766328), which is freely accessible to the public, and a part of the DataONE network registered with fairsharing.org.

References

46. Kendall, K. A., Shanley, J. B. & McDonnell, J. J. A hydrometric and geochemical approach to test the transmissivity feedback hypothesis during snowmelt. *J. Hydrol.* **219**, 188–205 (1999).
47. Brooks, E. S., Boll, J. & McDaniel, P. A. A hillslope-scale experiment to measure lateral saturated hydraulic conductivity. *Water Resour. Res.* **40**, W04208 (2004).
48. Moldrup, P. et al. Predicting the gas diffusion coefficient in repacked soil: water-induced linear reduction model. *Soil Sci. Soc. Am. J.* **64**, 1588–1594 (2000).
49. Massman, W. J. A review of the molecular diffusivities of H_2O, CO_2, CH_4, CO, O_3, SO_2, NH_3, N_2O, NO, and NO_2 in air, O_2 and N_2 near STP. *Atmos. Environ.* **32**, 1111–1127 (1998).
50. Bowling, D. R. & Massman, W. J. Persistent wind-induced enhancement of diffusive CO_2 transport in a mountain forest snowpack. *J. Geophys. Res. Biogeosci.* **116**, G04006 (2011).

Acknowledgements

The authors thank Rocky Mountain Biological Laboratory (RMBL) for helping with field research. This work was conducted as part of the Watershed Function Scientific Focus Area at Lawrence Berkeley National Laboratory and was supported by the US Department of Energy (DOE) Subsurface Biogeochemical Research Program, DOE Office of Science, Office of Biological and Environmental Research, under contract no. DE-AC0$_2$−05CH11231. Mention of trade names and commercial analytical services does not imply endorsement.

Author contributions

J.W. and T.K.T. designed the research, conducted the data analyses and wrote the manuscript; K.H.W. led the field team; T.K.T., K.H.W., A.W.N., W.B., C.A.B. and A.N.H. performed field instrumentation, monitoring and sampling; J.W., W.D., M.B., N.H.-C., M.E.C. and N.J.B. conducted laboratory measurements. S.S.H. contributed to the conceptual model and reviewed the manuscript.

Competing interests

The authors declare no competing interests.

Additional information

Extended data is available for this paper at https://doi.org/10.1038/s41561-021-00717-0.

Correspondence and requests for materials should be addressed to J.W. or T.K.T.

Peer review information *Nature Geoscience* thanks Nina Bingham, JoAnn Holloway and the other, anonymous, reviewer(s) for their contribution to the peer review of this work. Primary Handling Editor: Rebecca Neely.

Reprints and permissions information is available at www.nature.com/reprints.

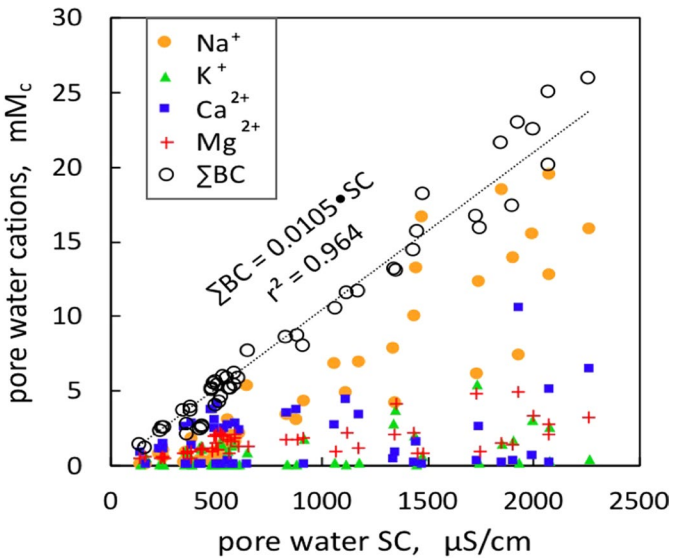

Extended Data Fig. 1 | Correlations between the sum of separately measured base cations (∑BC) and the specific conductance (SC) in porewaters. The measured SC values were used for weathering rates calculations.

	zone	K $m\ s^{-1}$	% of yearly N exported during maximum 2 months	TDN export rates: per unit transect width $mol\ m^{-1}\ y^{-1}$	TDN per transect area $mol\ ha^{-1}\ y^{-1}$	TDN per transect area $kg\ ha^{-1}\ y^{-1}$
measured K	surf. soil	9.70×10^{-6}		0.22	4.5	0.06
	subsoil	7.90×10^{-6}				
	WZ	1.10×10^{-5}		22.7	471	6.60
	FBR	1.60×10^{-7}		9.8	203	2.84
	total subsurface exports			32.7	678	9.49
	% of yearly N exported during maximum 2 months		39%			
enhanced K for soil and WZ	soil	2.42×10^{-4}		5.4	113	1.6
	subsoil	1.98×10^{-4}				
	WZ	1.65×10^{-5}		34.2	710	9.9
	FBR	1.60×10^{-7}		1.5	31	0.4
	total subsurface exports			40.7	845	11.8
	% of yearly N exported during maximum 2 months		49%			

Extended Data Fig. 2 | Summary of calculated subsurface total dissolved nitrogen (TDN export rates). The TDN concentrations and export rates are averaged from May 2017 to September 2019. Predictions using flow rates based on field-measured *K* and enhanced *K* (25x for soil, 1.5x for the WZ) are compared. In the table, WZ and FBR refer to the weathering zone and fractured bedrock, respectively. The importance of TDN export during the peak 2-month periods of snowmelt recharge is noteworthy, amounting to 39% and 49% of total exports, based on the measured and enhance *K*, respectively.

	measured *K*	enhanced *K*	average transport	measured *K*	enhanced *K*	average transport
	Import/Export rate Kg N ha^{-1} y^{-1}			fraction of import or export		
atmospheric dep.	2.7	2.7	2.7	0.114	0.108	0.11
biological N-fix.	2.7	2.7	2.7	0.114	0.108	0.11
rock weathering N	18.1	19.6	18.9	0.77	0.78	0.78
porewater export	-9.5	-11.8	-10.6	-0.39	-0.49	-0.44
N_2 + N_2O flux	-14.0	-13.2	-13.6	-0.58	-0.54	-0.56
N_2O flux			-3.5			-0.14

Extended Data Fig. 3 | Hillslope N mass balance. Nitrogen fluxes along the lower montane hillslope. The two different hydraulic conductivity (*K*) scenarios constrain N influxes from weathering and effluxes in groundwater flow and overall diffusion ($N_2 + N_2O$) to the atmosphere. The N_2O flux is the three-year average of diffusion calculations with and without inclusion of winter 2018–2019, for three locations.